JℲM PAPERS

Fingering instability in wildfire fronts

S.J. Harris[1],† and N.R. McDonald[1]

[1]Department of Mathematics, University College London Gower Street, London WC1E 6BT, UK

A two-dimensional model for the evolution of the fire line – the interface between burned and unburned regions of a wildfire – is formulated. The fire line normal velocity has three contributions: (i) a constant rate of spread representing convection and radiation effects; (ii) a curvature term that smooths the fire line; and (iii) a Stefan-like term in the direction of the oxygen gradient. While the first two effects are geometrical, (iii) is dynamical and requires the solution of the steady advection–diffusion equation for oxygen, with advection owing to a self-induced 'fire wind', modelled by the gradient of a harmonic potential field. The conformal invariance of this coupled pair of partial differential equations, which has the Péclet number Pe as its only parameter, is exploited to compute numerically the evolution of both radial and infinitely long periodic fire lines. A linear stability analysis shows that fire line instability is possible, dependent on the ratio of curvature to oxygen effects. Unstable fire lines develop finger-like protrusions into the unburned region; the geometry of these fingers is varied and depends on the relative magnitudes of (i)–(iii). It is argued that for radial fires, the fire wind strength scales with the fire's effective radius, meaning that Pe increases in time, so all fire lines eventually become unstable. For periodic fire lines, Pe remains constant, so fire line stability is possible. The results of this study provide a possible explanation for the formation of fire fingers observed in wildfires.

Key words: fingering instability, combustion

1. Introduction

Recent years have seen a marked increase in large-scale destructive wildfires in many regions, including North America, Siberia, Australia and Europe. This is consistent with the study of Jolly *et al.* (2015), who use an annual metric measuring 'fire weather' season length to show an 18.7 % increase in global mean fire weather season length over the period 1979 to 2013. The 2021 Intergovernmental Panel on Climate Change (IPCC)

† Email address for correspondence: sam.harris.16@ucl.ac.uk

report (Masson-Delmotte *et al.* 2021) predicts further increases of fire weather conditions. Understanding the dynamics of wildfires is therefore becoming increasingly vital. From a fluid mechanics perspective, wildfires are complex, involving physical, chemical and thermodynamic processes, and their interaction with environmental factors such as winds, vegetation and topography. A variety of approaches aimed at understanding wildfires have been adopted, including empirical, statistical and physical modelling, with methods spanning experimental, observational, mathematical and computational techniques. Many of these previous works are summarised in the review articles of Perry (1998), Pastor *et al.* (2003), Sullivan (2009*a*,*b*,*c*) and Bakhshaii & Johnson (2019).

Minimising the risks and impacts of wildfires requires predicting the behaviour of the spreading fire line. In this work, the fire line is taken to be the interface between burned and unburned regions, and how this interface evolves on a two-dimensional surface – the land surface – is a key question. Mathematically, the problem is the geometric evolution of a two-dimensional non-intersecting curve in which the normal velocity at a point on the curve is either prescribed or needs to be determined according to a physical model for the fire line evolution.

An essential ingredient to wildfire spread is the availability of oxygen. The processes and effects in which oxygen additional to that otherwise available in calm conditions is fed to the fire by fire-induced wind (the 'fire wind', also known as pyrogenic wind/flow, see Hilton *et al.* 2018) are the subject of this study. Buoyant upflow over the burned region creates local low pressure, which in turn acts as a sink, drawing in surrounding air in a shallow ground-level layer and so generating fire wind (Smith, Morton & Leslie 1975). Beer (1991) presents a stoichiometric argument that the oxygen necessary for combustion must be supplied by turbulent mixing from an inward horizontal flow. In calm conditions, this requirement leads to the generation of fire wind. It is interesting to note that Beer (1991) also shows that when an ambient wind is present (which the present study does not consider), it will supply the sufficient oxygen needed for combustion, so there is little reason to expect fire wind in the case of a wind-driven fire. However, fire winds of velocities up to 3 m s^{-1} have been observed for even modest-sized ($\approx$ 2 km radius in the horizontal direction) wildfires (e.g. Lareau & Clements 2017). In their numerical simulation of the 1991 Oakland Hills fire, Trelles & Pagni (1997) found that the fire wind rapidly increased from 2.6 m s^{-1} to 13.0 m s^{-1} as the fire intensified. Moreover, they found that the horizontal fire-induced wind was drawn towards the centroid of multiple fire plumes.

This paper formulates a simple two-dimensional model for the effect of fire wind on wildfires, which is used to investigate fire line stability and its nonlinear evolution. The model assumes that the oxygen concentration in the unbounded region exterior to the fire is governed by the steady advection–diffusion equation, with advective transport effected by the fire wind. This fire wind, modelled by a two-dimensional potential flow, brings in oxygen-rich air from infinity for consumption by the fire at the fire line. In response, the fire line velocity is proportional to the normal gradient of oxygen at the fire line, in the direction of its outward normal. As such, the fire line is susceptible to the Mullins–Sekerka instability (Mullins & Sekerka 1964) and, as will be shown, may develop finger-like protrusions.

The steady two-dimensional advection–diffusion equation and Laplace equation, which govern the oxygen transport and fluid flow, respectively, are a pair of conformally invariant partial differential equations (PDEs) (Cummings *et al.* 1999; Bazant 2004) – a property that is exploited in the numerical method. The infinite unburned region, with boundary representing the fire line, is represented as a conformal map from the unit

disk in some 'mathematical' plane. The free-boundary problem for the unknown fire line then becomes that of determining the conformal map using a Polubarinova–Galin type equation (Gustafsson & Vasil'ev 2006). Similar approaches have been used in both the analytical and numerical solutions of Hele-Shaw free-boundary problems (e.g. Howison 1986; Dallaston & McCue 2013; Miranda & Widom 1998) and determining the evolution of two-dimensional freezing, melting or dissolution of bodies in two-dimensional potential flows (e.g. Cummings *et al.* 1999; Rycroft & Bazant 2016; Ladd, Yu & Szymczak 2020).

Fire lines have been observed to develop 'fingering' instabilities. Clark *et al.* (1996*a*) discuss the 1985 Onion sage brush fire in Owens Valley, California, where the fire line developed multiple protrusions spaced about 1 km apart (see their figure 1). Clark *et al.* (1996*a*) used a three-dimensional coupled fire-atmosphere numerical model to attribute finger formation to feedback between the hot convective plume and the near-surface convergence at the fire line. However, there is no oxygen effect in their simulations, and the fingering mechanism is owing to vorticity generation and the breakup of the buoyancy-driven plume into smaller cells (see also Clark *et al.* 1996*b*). Dold, Sivashinsky & Weber (2005) also propose a dynamic model for fire line instability linked to the presence of a hot plume over the fire. The plume partially blocks incoming airflow and, along with a stably stratified atmosphere, the overall effect is to accelerate incoming air in the direction normal to the fire line. They use a stability analysis to argue that perturbations to the fire line grow owing to an increased airflow, hence increased burning rate, at the more advanced parts of the front. Although not mentioned explicitly, the Dold *et al.* (2005) assumption that the burn rate, or fire line speed, is proportional to the oncoming airflow feeding the fire appears analogous to the oxygen effect considered in this paper. Recently, Quaife & Speer (2021) used a two-dimensional, reduced physics, cellular automata model of fire-atmosphere interaction incorporating a fire-plume-induced convective sink, and vorticity sources at the flanks of the fire. Amongst a variety of fire line behaviours observed in their model was fingering, in the form of the breakup of the fire line into multiple advancing heads.

Previous works that consider explicitly the effects of oxygen transport in producing fingering instability in combustion are the experimental investigations by Zik, Olami & Moses (1998) and Zik & Moses (1999), and the numerical work of Conti & Marconi (2002, 2010). The former describe experiments in which solid fuel in a Hele-Shaw cell is forced to burn against an oxidising wind. A fingering instability is observed with two decoupled length scales: the finger width and the inter-finger distance, the latter being determined by the Péclet number measuring the relative importance of oxygen and diffusion. Motivated by these experiments, Kagan & Sivashinsky (2008) derive a nonlinear PDE that models the free boundary between the solid fuel and air, demonstrating that the fingering is similar to the instability occurring in premixed gas flames. Conti & Marconi (2002, 2010) use a numerical lattice model to consider the diffusion of both heat and oxygen at advancing fire fronts. Fingering is observed, with the nonlinear evolution of the front developing into either a cellular or a dendritic pattern, depending on the parameters chosen, e.g. the initial oxygen concentration.

The structure of this paper is as follows. In § 2, the simplified model of fire line growth, incorporating the effects of oxygen advection and diffusion, is formulated for radial fires. The fire burns on a flat surface with uniform combustible fuel that, typically, is some form of vegetation, e.g. grass or heathland. The only wind present is the self-induced fire wind. In addition to the oxygen effect, the fire line velocity is assumed to have two other contributions. The first is a constant fire line velocity owing to the cumulative effect of radiation and convection. Determining fire line velocity from these effects alone is in itself

a complex and difficult problem, with the comparative roles of convection and radiation still an active area of research (e.g. Finney *et al.* 2015). Here, following e.g. Hilton *et al.* (2016, 2018), it is assumed simply that radiation and convection, together with fuel type and the background level of oxygen, give rise to a constant fire line velocity v_0 (the 'rate of spread', or ROS) in a direction normal to the fire line. The second contribution is the effect of the curvature of the fire line: curvature acts to increase the propagation of concave regions of the fire line, since more heat is able to be transferred into such unburned regions. This causes faster ignition of the fuel compared to regions outside of convex fire line segments, which transfer heat to a wider, and so larger, area of unburned fuel (Markstein 1951; Sethian 1985; Sharples *et al.* 2013; Wheeler *et al.* 2015; Hilton *et al.* 2016). Consequently, curvature stabilises, or smooths out, perturbations, in this sense acting in the same way as 'curve-shortening' (Gage & Hamilton 1986; Grayson 1987; Dallaston & McCue 2016).

The linear stability of the fire line is investigated in § 3, quantifying its dependence on wavenumber, ROS, curvature and the Péclet number. Nonlinear evolution, including finger formation, of perturbed circular fire lines is then computed numerically using the conformal mapping approach in § 4, along with a derivation of a law for the rate of change of area of the burned region, which serves as a useful check on the numerical results. Periodic planar fire lines are considered in § 5; this is analogous to studying a large wildfire at a local scale. Finally, § 6 provides a discussion of the results obtained from this paper and their application to wildfires.

2. Radial fire model

The radial wildfire problem is illustrated in figure 1, where figure 1(*a*) gives a top-down (plan) view of the wildfire, and 1(*b*) gives a side view. Consider a two-dimensional, non-overlapping, finite curve γ – the fire line – enclosing a region R of burned fuel, where the unburned region Ω is the (x, y)-plane punctured by R, and the fire line is traversed with R on the left. It is assumed that a single bone-dry fuel type is used, distributed uniformly on flat terrain with zero ambient wind; the only wind present is a self-induced 'pyrogenic (fire) wind'. Smith *et al.* (1975) discuss in detail the role of dynamic pressure in generating this fire wind; using a numerical model, they show that the strong buoyant acceleration over the fire region generates locally low pressure, leading to a horizontal pressure gradient that in turn generates the pyrogenic wind (Hilton *et al.* 2018). This strong inflow is quite different in nature to the relatively weak, entraining inflows associated commonly with turbulent plume dynamics, and is best modelled using dynamic pressure, which communicates the effect of fire-driven buoyant air to the surrounding fluid. Pressure anomalies to model fire-driven surface winds have been used previously (e.g. Achtemeier 2012). Once the fire wind reaches the fire line, a proportion of its oxygen is used in combustion (Beer 1991) before the air enters the burned region and is ejected from the system.

It is assumed that the fire wind is a two-dimensional horizontal flow occurring in a shallow layer of depth H in the unburned region Ω parallel to the ground surface; see figure 1(*b*). The layer depth H is much smaller than the horizontal length scale of the fire. Defining the Reynolds number $Re = UH/D$, where U is a typical fire wind velocity at the fire line and D is the momentum diffusivity for turbulent flow, and using values typical for a small starting fire – $U \sim 0.025$ m s^{-1}, $H \sim 10$m and $D \sim 1$ m^2 s^{-1} (Bebieva *et al.* 2020) – gives $Re \approx 0.25$. Thus, to a reasonable approximation, the Stokes flow equations govern the flow in the shallow layer exterior to the fire. This approximation 'improves' further from the fire where the inflow velocity decreases. However, as the fire intensifies, the
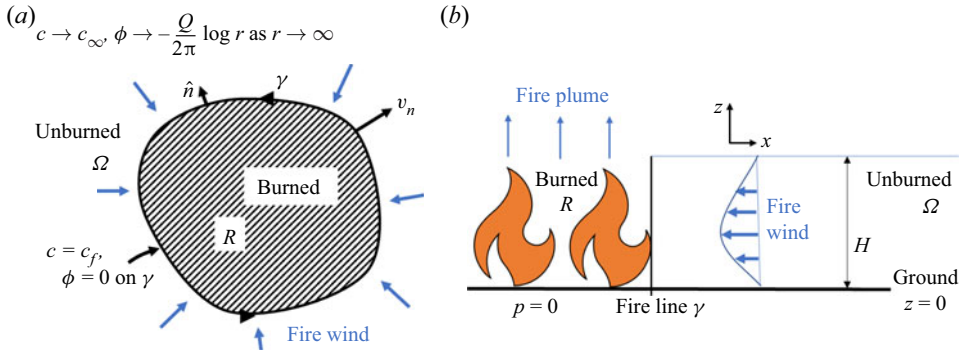
Figure 1. The radial wildfire model: (*a*) plan view; (*b*) side view. The blue arrows represent the direction of the fire wind governed by the potential ϕ.

velocity scale U will increase, leading to an increase in Re, but this increase may be offset due to an expected increase in the diffusion coefficient D, owing to increased turbulent mixing. Assuming that the approximation remains reasonable, such shallow flows are analogous to those in a Hele-Shaw cell, and a standard derivation involving integration of the Stokes equations over the layer depth (see e.g. Gustafsson & Vasil'ev 2006) shows that $u = \nabla \phi \sim -\nabla p$, where the velocity potential ϕ is proportional to the (negative) pressure p. Note that u is the average fire wind velocity over H. Without loss of generality, in the present work, the low pressure over the fire is represented by taking $\phi = 0$ over the fire, and on γ in particular.

The fluid is incompressible and, to good agreement with experimental data (Hilton *et al.* 2018), the wind can also be treated as irrotational, so ϕ satisfies the Laplace equation

$$\nabla^2 \phi = 0 \quad \text{in } \Omega. \tag{2.1}$$

Irrespective of the assumptions made here, modelling the flow exterior to wildfires and plumes using solutions of the two-dimensional Laplace equation has been used previously by e.g. Weihs & Small (1986), Maynard, Princevac & Weise (2016), Sharples & Hilton (2020), Quaife & Speer (2021) and Kaye & Linden (2004).

Further, it is assumed that the fire wind velocity u is much larger than the normal velocity v_n of the fire line, so the system is quasi-steady. The oxygen concentration c thus satisfies the steady advection–diffusion equation

$$u \cdot \nabla c = D \nabla^2 c \quad \text{in } \Omega, \tag{2.2}$$

where D is the diffusivity of c. Equations (2.1) and (2.2) form a coupled system to be solved, with suitable boundary and far-field conditions needed.

The background oxygen concentration far from the fire, $r \to \infty$, is denoted $c = c_\infty$, and is $c = c_f$ on the fire line γ itself. This latter condition results from an assumption that the fire is uniform in its intensity at points around the fire line, and consumes oxygen to the same level; the actual value of $c_f < c_\infty$ is immaterial. Specification of such a Dirichlet boundary condition on the moving interface for the quantity undergoing advection and diffusion is used in other moving-boundary problems, e.g. in Cummings *et al.* (1999) and Tsai & Wettlaufer (2007).

The low pressure at the fire plume appears as an effective sink in the far field, so the velocity potential has behaviour $\phi = -(Q/2\pi) \log r$ in the far-field, where $Q > 0$ is the strength of the sink. Note that as the fire expands and intensifies over time, the ability

of the fire plume to draw in surrounding air increases, thus the sink strength Q also increases over time, leading to a larger fire wind flux (Trelles & Pagni 1997). Therefore, let $Q = Q(t) = Q_0 \, q(t)$, where $q(0) = 1$, and Q_0 is some constant. The implications of this are considered further throughout this paper. To summarise, the boundary and far-field conditions for the velocity potential ϕ and the oxygen concentration c are

$$c = c_f, \quad \phi = 0 \quad \text{on } \gamma, \qquad (2.3a,b)$$

$$c \to c_\infty, \quad \phi \to -\frac{Q(t)}{2\pi} \log r \quad \text{as } r \to \infty. \qquad (2.4a,b)$$

The velocity v_n of the fire line γ in the direction of the outward unit normal $\hat{\boldsymbol{n}}$ is sought. Markstein (1951) first proposed a simple model for the velocity v_n of flame fronts, which showed qualitatively good agreement with experimental data. The model reads as

$$v_n = v_0 - \delta \kappa. \qquad (2.5)$$

The constant v_0 is the basic rate of spread (ROS), a parameter quantifying the physical properties of the fuel, e.g. the speed at which fuel ignites under heating, and the heat transferred by radiation and convection from burning to unburned fuel cells. While there is ongoing research in quantifying v_0 for different fuel types (Sullivan 2009a; Finney *et al.* 2015), v_0 is treated simply as some constant here. Markstein (1951) found that the correction term $-\delta \kappa$ was needed for better matching with experimental results, where κ is the (signed) curvature, and δ is a constant, with $\delta \ll v_0$. Note that (2.5) is a type of curve-shortening (or in this context curve-lengthening) equation (e.g. Grayson 1987; Dallaston & McCue 2016). Physically, (2.5) acts to smooth out perturbations in the fire line; concave sections of the fire line grow faster as more heat is transferred to the unburned regions of fuel that these sections enclose. The geometric wildfire model (2.5) has been studied previously by e.g. Sethian (1985) and Sharples *et al.* (2013); the latter simulated successfully the propagation of fire junctions using the model.

The purely geometric rule (2.5) does not lead to the sometimes observed phenomenon of wildfire fingering (Clark *et al.* 1996a,b; Dold *et al.* 2005). Therefore, a dynamical oxygen effect is introduced into v_n in which the interface velocity is dependent on the gradient of c in the normal direction, i.e. $v_n = \partial c / \partial n$. This additional term simulates the expected behaviour: the fire grows preferentially in the direction of higher oxygen concentration (the closer the fire line is to the source of oxygen, the more quickly combustion can occur and hence the faster the fire line propagates), which can result in fire fingering. In particular, the equation for v_n is written as

$$v_n = v_0 - \delta \kappa + \alpha \hat{\boldsymbol{n}} \cdot \nabla c \quad \text{on } \gamma, \qquad (2.6)$$

where α is some constant. Whilst v_0 is a constant and the curvature κ is a geometrical property of the fire line, $\hat{\boldsymbol{n}} \cdot \nabla c$ is dynamical and requires the solution for the oxygen concentration c. This is found by solving the system (2.1)–(2.4a,b).

2.1. *Non-dimensionalisation and the Péclet number*

The system (2.1)–(2.4a,b) and (2.6) is now non-dimensionalised. First, the length scale L is chosen to be the initial radius $L = R_0$ of the wildfire. Scalings are then chosen to give rise to an $O(1)$ oxygen-driven contribution to v_n, since oxygen effects are of particular

interest in this study. Thus the dimensionless (starred) variables are

$$\nabla = \frac{1}{L}\nabla^*, \quad \phi = \frac{Q}{2\pi}\phi^*, \quad c^* = \frac{c - c_f}{c_\infty - c_f}, \quad t = \frac{L}{U\,Pe_0}t^*, \quad U = \frac{\alpha(c_\infty - c_f)}{L},$$

(2.7a–e)

where $Pe_0 = Q_0/2\pi D$, for $Q_0 = Q(0)$, is the constant initial value of the Péclet number. The non-dimensional system for the wildfire problem, after dropping the stars, is

$$Pe_0\, v_n = V_0 - \bar{\epsilon}\kappa + \hat{\boldsymbol{n}} \cdot \nabla c \quad \text{on } \gamma, \tag{2.8}$$

$$\nabla^2\phi = 0 \quad \text{in } \Omega, \tag{2.9}$$

$$Pe\,\boldsymbol{u} \cdot \nabla c = \nabla^2 c \quad \text{in } \Omega, \tag{2.10}$$

$$c = 0, \quad \phi = 0 \quad \text{on } \gamma, \tag{2.11a,b}$$

$$c \to 1, \quad \phi \to -\log r \quad \text{as } r \to \infty. \tag{2.12a,b}$$

where the new dimensionless constants V_0 and $\bar{\epsilon}$, representing the ROS and magnitude of the curvature effect, respectively, are

$$V_0 = \frac{Lv_0}{\alpha(c_\infty - c_f)}, \quad \bar{\epsilon} = \frac{\delta}{\alpha(c_\infty - c_f)}. \tag{2.13a,b}$$

Note that the non-dimensional time-varying, Péclet number Pe now appears in (2.10) and is

$$Pe = \frac{Q(t)}{2\pi D} = \frac{Q_0\,q(t)}{2\pi D} = Pe_0\,q(t). \tag{2.14}$$

Recall that the plume strength $Q(t) = Q_0\,q(t)$ is assumed to grow in time as the fire expands, thus the Péclet number also increases in time. Choosing $q(t) \sim R(t)$, where $R(t)$ is the radius of the burned region R, gives

$$Pe = \frac{Pe_0}{R_0}R(t). \tag{2.15}$$

For all numerical experiments reported here, $R_0 = 1$, so the Péclet number is simply $Pe = Pe_0\,R(t)$. Note also that Pe_0 has been incorporated in the scale for time t^* in (2.7a–e).

Finally, note that it is required on physical grounds that the fire always progresses from the burned region R into the unburned region Ω; this is known as the entropy condition (Sethian 1985). There is no explicit mechanism in the wildfire model (2.9)–(2.12) to enforce this entropy condition. This does not affect the linear stability results of § 3, since the fire line does not move, but such unphysical behaviour is possible in the nonlinear evolution of the fire line computed in § 4. In practice, this is likely to be rare, since both the V_0 and $\hat{\boldsymbol{n}} \cdot \nabla c$ terms cause the fire line to propagate towards the unburned region, and $\bar{\epsilon}$ is taken to be small in comparison since, as you may recall, $\delta \ll v_0$ and hence $\bar{\epsilon} \ll V_0$.

3. Stability analysis

The stability of a perturbed curve γ evolving under the system (2.8)–(2.12) is studied. Such stability is determined by the competing effects of curvature (stabilising) and oxygen consumption (destabilising), quantified by the parameters $\bar{\epsilon}$ and Pe, respectively. It is expected that there is some range of wavenumbers that grow over time, hence are unstable, for certain choices of $\bar{\epsilon}$ and Pe.

First, consider an unperturbed base state γ given by the circle $r = R(t)$, with $R(0) = 1$, so that $Pe = Pe_0 R(t)$. The solution to (2.9)–(2.12) is

$$\phi(r) = -\log\frac{r}{R}, \quad c(r) = 1 - \left(\frac{R}{r}\right)^{Pe}. \tag{3.1a,b}$$

Since the curvature for a circle of radius R is $\kappa = R^{-1}$, (2.8) gives the normal velocity of γ as

$$Pe_0\, v_n = Pe_0\,\dot{R} = V_0 - \frac{\bar{\epsilon}}{R} + \frac{Pe}{R}, \tag{3.2}$$

where the dot denotes the time derivative. Dividing through by Pe gives the relative growth of radius R:

$$\frac{\dot{R}}{R} = \frac{V_0}{Pe_0\, R} - \frac{\sigma}{R} + \frac{1}{R} = \frac{1}{R}\left[\frac{V_0}{Pe_0} - \sigma + 1\right], \tag{3.3}$$

where $\sigma = \sigma(t) = \bar{\epsilon}/Pe$. Therefore, provided that $\bar{\epsilon} < V_0 + Pe_0$ (which is necessarily true as $\bar{\epsilon} \ll V_0$), $R(t)$ and hence also the Péclet number grow in time.

Now consider the perturbed circular fire line

$$r = r_p = R(t) + \sum_{n=1}^{\infty} \delta_n(t) \cos n\theta, \tag{3.4}$$

where $\delta_n \ll 1$, for all n. The summation sign is dropped henceforth. Note that the $n = 1$ mode corresponds to a uniform translation of the fire line (Brower *et al.* 1984) and is stable, so only the stability of perturbations $n \geqslant 2$ is considered.

The following expression for ϕ solves the Laplace equation (2.9) and satisfies the far-field condition (2.12*b*):

$$\phi = -\log\frac{r}{R} + \beta_n \frac{R^n}{r^n} \cos n\theta, \tag{3.5}$$

where $\beta_n \ll 1$ is a constant. Equations (3.1*a,b*) and (3.5) suggest writing

$$c = 1 - \left(\frac{R}{r}\right)^{Pe} + \gamma_n \frac{R^{\alpha_n}}{r^{\alpha_n}} \cos n\theta, \tag{3.6}$$

where $\gamma_n \ll 1$ and $\alpha_n > 0$ are constants. Note that (3.6) satisfies the far-field condition (2.12*a*). The condition (2.11*a,b*) gives $\beta_n = \delta_n/R$ and $\gamma_n = -Pe\delta_n/R$. Substituting (3.5) and (3.6) into (2.10), and retaining terms to $O(\delta_n)$, it follows that $\alpha_n = n + Pe$.

The normal velocity (2.8) on $r = r_p$ can now be obtained to $O(\delta_n^2)$. Note that

$$v_n = \frac{\partial \boldsymbol{x}}{\partial t} \cdot \hat{\boldsymbol{n}} = \dot{R} + \dot{\delta}_n \cos n\theta + O(\delta_n^2), \tag{3.7}$$

$$\kappa = \frac{1}{R}\left[1 + \frac{\delta_n(n^2 - 1)}{R}\cos n\theta\right] + O(\delta_n^2), \tag{3.8}$$

$$\hat{\boldsymbol{n}} \cdot \nabla c = \frac{\partial c}{\partial r} + O(\delta_n^2) = \frac{Pe}{R}\left[1 + \frac{\delta_n(n - 1)}{R}\cos n\theta\right] + O(\delta_n^2). \tag{3.9}$$

Evaluating (2.8) gives

$$Pe_0 \left(\dot{R} + \dot{\delta}_n \cos n\theta \right) = V_0 + \frac{1}{R} \left[-\bar{\epsilon} + Pe + \frac{\delta_n}{R} \left(-\bar{\epsilon}(n^2 - 1) + Pe(n - 1) \right) \cos n\theta \right] + O(\delta_n^2). \tag{3.10}$$

The leading-order term of (3.10) is a restatement of (3.3). To $O(\delta_n)$, the growth rate for the nth mode of perturbation is

$$\frac{\dot{\delta}_n}{\delta_n} = \frac{1}{R} \left[-\sigma n^2 + n + (\sigma - 1) \right]. \tag{3.11}$$

The difference between (3.11) and (3.3) gives the growth of perturbations relative to the overall growth of the wildfire. This is an important distinction to make, as if perturbations grow slower than the radius R, then the observed behaviour is that of stability (see also Dallaston & Hewitt 2014). A measure of the relative growth rate is

$$g(n) = \frac{\partial}{\partial t} \left(\log \left(\frac{\delta_n}{R} \right) \right) = \frac{\dot{\delta}_n}{\delta_n} - \frac{\dot{R}}{R} = \frac{1}{R} \left(-\sigma n^2 + n + 2(\sigma - 1) - \lambda \right), \tag{3.12}$$

where $\lambda = V_0 / Pe_0$. Instability occurs when $g(n) > 0$. If $\sigma = 0$, i.e. $\bar{\epsilon} = 0$ (zero curvature effect), then $g(n) = (n - 2 - \lambda)/R$, and all modes $n > 2 + \lambda$ are unstable. However, if the initial Péclet number is very small, then $\sigma, \lambda \to \infty$ and $g(n) \to (\sigma(2 - n^2) - \lambda)/R$, so all modes $n \geqslant 2$ are stable. This demonstrates that both stable and unstable fire line behaviour are possible.

The stability of perturbations depends on the sign of the numerator of (3.12),

$$f(n) = -\sigma n^2 + n + 2(\sigma - 1) - \lambda, \tag{3.13}$$

which is such that $f(n) > 0$ for $n_- < n < n_+$, where

$$n_\pm = \frac{1 \pm \sqrt{\Delta}}{2\sigma}, \quad \Delta = 8\sigma^2 - 4\sigma(2 + \lambda) + 1. \tag{3.14a,b}$$

Real roots $n_\pm$ exist when $\Delta > 0$. Note that if $\Delta = 0$, then $n_- = n_+ = n^*$ and $f(n^*) = 0$, which is stable. The function Δ is positive for $\sigma_- > \sigma$ and $\sigma_+ < \sigma$, where

$$\sigma_\pm = \frac{2 + \lambda \pm \sqrt{\lambda^2 + 4\lambda + 2}}{4}. \tag{3.15}$$

As $\lambda > 0$, these roots always exist, and if $\sigma_- \leqslant \sigma \leqslant \sigma_+$, then all modes are stable. Noting that $\sigma_- > 0$, the instability region $\sigma_- > \sigma$ is observable for $\sigma > 0$. However, the limit $\sigma \to \infty$ gives $n_+ < 2$, hence the instability region $\sigma > \sigma_+$ is generally not observable. Finally, differentiating (3.12) with respect to n finds the maximum growth rate g_{max} as

$$n_{max} = \frac{1}{2\sigma}, \quad g_{max} = \frac{1}{R} \left(\frac{1}{4\sigma} + 2(\sigma - 1) - \lambda \right), \tag{3.16a,b}$$

where n_{max} is the mode of perturbation corresponding to g_{max}. If all modes of perturbation are stable, then g_{max} is the slowest rate of decay. In an unstable regime, the fastest growing mode n_{max} becomes the dominant perturbation, but as σ decreases in time (since $Pe = Pe_0 R(t)$ increases as the fire expands), the dominant mode n_{max} also changes. This behaviour is explored in §4.
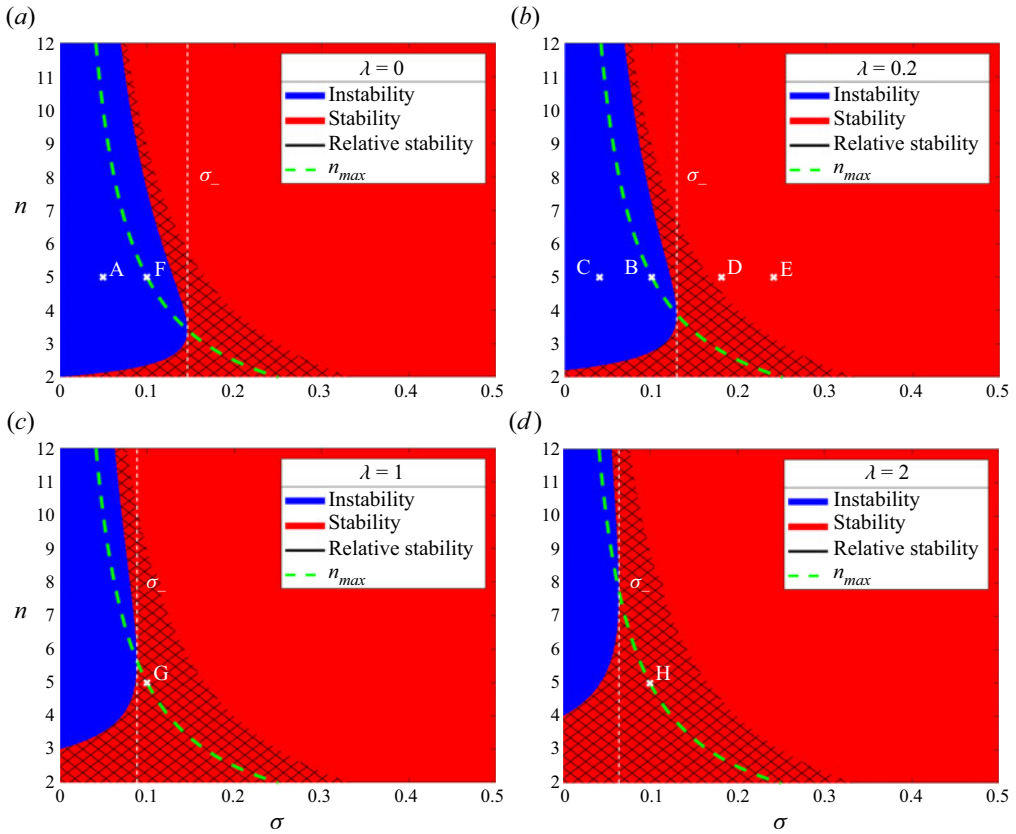
Figure 2. Parameter space stability diagrams for the perturbed fire line (3.4). Regions of instability are in blue, regions of stability are in red, and the cross-hatched areas (denoted by the black line in the graph key) are regions of 'relative stability'. The points A–H correspond to initial choices of σ and n in figures in § 4 as follows: A – figure 3; B – figures 4, 5(b), 7(b); C – figure 5(a); D – figure 5(c); E – figure 5(d); F – figure 7(a); G – figure 7(c); H – figure 7(d).

For a given value of $\lambda = V_0/Pe_0$, a (σ, n) parameter space stability diagram can be constructed as in figure 2. Regions of instability ($g(n) > 0$, blue) and stability ($g(n) \leqslant 0$, red) are shaded, along with a cross-hatched area in the red stability region where perturbations grow but are outpaced by the growing radius of the fire line. Four such stability diagrams are given in figure 2, the points A–H corresponding to initial σ and n values for specified numerical results in § 4. It is important to note that as σ decreases over time, the points A–H will propagate to the left as t increases. This is also discussed in § 4.

4. Numerical simulation of nonlinear evolution

4.1. *Conformal mapping method*

A numerical method based on conformal mapping is used to compute the nonlinear evolution of the fire line γ. Let $z = f(\zeta, t)$ map the interior of the unit ζ-disk to Ω, with $\zeta = 0$ mapping to infinity. Conformal invariance of (2.9) and (2.10), along with boundary conditions $\phi \to \log |\zeta|$, $c = 1$ as $\zeta \to 0$, and $\phi = 0$, $c = 0$ on $|\zeta| = 1$, enables solutions

943 A34-10

for ϕ and c to be found in the ζ-plane:

$$\phi(\zeta) = \log|\zeta|, \quad c(\zeta) = 1 - |\zeta|^{Pe}. \tag{4.1a,b}$$

The numerical task is now to find the conformal map $z = f(\zeta, t)$. As in other free-boundary problems such as Hele-Shaw flow and dissolution of solids in potential flow, the kinematic condition (2.8) is formulated in terms of the conformal map $z = f(\zeta, t)$, yielding an equation of the Polubarinova–Galin class (e.g. Howison 1986; Ladd *et al.* 2020).

Write the unknown map as

$$z = f(\zeta, t) = a_{-1}(t)\,\zeta^{-1} + \sum_{m=1}^{\infty} a_m(t)\,\zeta^{nm-1}, \tag{4.2}$$

where Ω is assumed to have *n*-fold symmetry, so the a_m are real, for all $m = -1, 1, 2, \ldots$, when $n \geqslant 1$. Note that a_{-1} is the conformal radius and is a measure of the horizontal length scale of the wild fire, thus is identical to $R(t)$ for a circular fire. Hence the Péclet number can be written as $Pe = Pe_0 R(t) = Pe_0 a_{-1}(t)$, where $a_{-1}(0) = 1$ is chosen in all numerical tests. The terms in (2.8) can be expressed in terms of the map (4.2). From Dallaston & McCue (2013),

$$v_n = \frac{\mathrm{Re}\left[f_t \overline{\zeta f_\zeta}\right]}{|f_\zeta|}, \quad \kappa = \frac{\mathrm{Re}\left[\zeta(\zeta f_\zeta)_\zeta \overline{\zeta f_\zeta}\right]}{|f_\zeta|^3}, \tag{4.3a,b}$$

and the oxygen concentration gradient is

$$\boldsymbol{n} \cdot \nabla c = \mathrm{Re}[n\,\bar{\nabla}c] = 2\,\mathrm{Re}\left[n\frac{\partial c}{\partial z}\right] = 2\,\mathrm{Re}\left[\frac{\zeta f_\zeta}{|f_\zeta|}\frac{\partial c}{\partial \zeta}\frac{1}{f_\zeta}\right] = -\frac{Pe}{|f_\zeta|} \quad \text{on } |\zeta| = 1, \tag{4.4}$$

where $\bar{\nabla} = 2\partial_z = \partial_x - i\partial_y$, $n = n_x + in_y$ is the complex representation of the normal vector in the *z*-plane, and $f_\zeta = \partial f/\partial \zeta$. Also used is the result $n = \zeta f_\zeta/|f_\zeta|$, and that c in the ζ-disk is given by (4.1a,b), so $\partial c/\partial \zeta = -Pe/2\zeta$ on $|\zeta| = 1$.

Now, (4.3a,b) and (4.4) can be substituted into (2.8), and multiplying through by $|f_\zeta|/Pe_0$ gives

$$\mathrm{Re}\left[f_t \overline{\zeta f_\zeta}\right] = -\frac{V_0}{Pe_0}|f_\zeta| + \frac{\bar{\epsilon}}{Pe_0}\frac{\mathrm{Re}\left[\zeta(\zeta f_\zeta)_\zeta \overline{\zeta f_\zeta}\right]}{|f_\zeta|^2} - a_{-1}(t). \tag{4.5}$$

Note that choosing $V_0 = \bar{\epsilon} = 0$ is analogous to the problem of viscous fingering of a fluid with zero surface tension in a Hele-Shaw cell (e.g. Howison 1986; Mineev-Weinstein 1998; Gustafsson & Vasil'ev 2006). Omitting the $a_{-1}(t)$ term in (4.5), i.e. when there is no oxygen effect, gives the wildfire model used in e.g. Markstein (1951) and Sharples *et al.* (2013), and is a variant of the curve-shortening problem considered by Dallaston & McCue (2016), except that, in this case, the sign of V_0 is such that the curve lengthens.

Following Dallaston & McCue (2013), the series in (4.2) is truncated at $m = N$, giving $N + 1$ unknown functions in time: $a_{-1}, a_1, \ldots, a_N$. Consequently, points $\zeta = \zeta_j$, $j = 1, \ldots, N + 1$, distributed uniformly around the ζ-disk, are chosen, so (4.2) becomes a system of $N + 1$ coupled first-order ODEs in t. Here, the MATLAB routine *ode15i* is used to solve this system.

4.2. *Rate of change of area law*

It is useful to find any identities satisfied by (2.8)–(2.12), as these can be used to assess the accuracy of the above numerical method. Let $A(t)$ be the area enclosed by the fire line

γ, and denote the length of γ by $L(t)$. The following geometrical properties of a smooth, non-intersecting, two-dimensional closed curve γ (Brower *et al.* 1984; Dallaston & McCue 2016) are used:

$$2\pi = \int_\gamma \kappa \, ds, \quad L(t) = \int_\gamma \, ds, \quad \frac{dA}{dt} = \int_\gamma v_n \, ds. \qquad (4.6a\text{–}c)$$

Substituting (2.8) into (4.6*c*) gives

$$\frac{dA}{dt} = \frac{V_0}{Pe_0} \int_\gamma \, ds - \frac{\bar{\epsilon}}{Pe_0} \int_\gamma \kappa \, ds + \frac{1}{Pe_0} \int_\gamma \frac{\partial c}{\partial n} \, ds. \qquad (4.7)$$

The first two terms on the right-hand side of (4.7) can be simplified using (4.6*a*,*b*). For the third term, first transform the integral to the unit ζ-disk $\zeta = e^{i\theta}$, where $0 \leqslant \theta < 2\pi$. Now use $\partial c / \partial n = Pe_0 \, a_{-1}(t) / |f_\zeta|$, which is similar to (4.4) but necessarily positive as the normal is directed outwards to γ. Since $ds = |f_\zeta| \, d\theta$, the rate of change of area law for the burned region is obtained:

$$\frac{dA}{dt} = \frac{V_0}{Pe_0} L(t) + 2\pi \left[a_{-1}(t) - \frac{\bar{\epsilon}}{Pe_0} \right]. \qquad (4.8)$$

The relation (4.8) is used to check the accuracy of the numerical results using the relative error

$$RE = \frac{\text{LHS} - \text{RHS}}{\text{RHS}}, \qquad (4.9)$$

where LHS and RHS are the left- and right-hand sides of (4.8), respectively.

4.3. *Results*

4.3.1. *Fire-stars*
The nonlinear evolution of a 5-fold symmetric shape ($n = 5$), or fire-star, is computed. First, consider the case with zero ROS, $V_0 = 0$, and small curvature effect, $\bar{\epsilon} = 0.1$. The initial Péclet number $Pe_0 = 2$ is chosen, thus $\lambda = V_0 / Pe_0 = 0$ and $\sigma_0 = \bar{\epsilon} / Pe_0 = 0.05$, corresponding to point A on the stability diagram figure 2(*a*). The series (4.2) is truncated at $N = 128$ terms, and the fire line evolves to $t_{max} = 1$; this evolution is shown in figure 3(*a*). Sections of the fire line penetrating the unburned region grow more quickly, and fingers develop from the tips of the initial perturbations. This behaviour is in agreement with the stability diagram, in which this evolution begins in the instability region and remains unstable as σ decreases over time, as a result of an increasing Péclet number. In addition, instability is also expected owing to the Mullins–Sekerka mechanism (Mullins & Sekerka 1964; Brower *et al.* 1984).

The relative error *RE* (see (4.9)) of the rate of change of area law (4.8) for figure 3(*a*) is plotted in figure 3(*b*). Each of the three plots corresponds to a different value of series truncation: $N = 32$, 64 and 128, where the higher the series truncation, the further in time the fire line can evolve before significant numerical errors appear. The cause of these errors is likely the lack of resolution in the 'valleys' of the fingers, due to a crowding of points at the 'finger tips'. While the points in the ζ-plane are distributed uniformly, when mapped with (4.2) to the z-plane, their distribution becomes non-uniform around the fire line, hence the crowding. Evolution with larger $\bar{\epsilon}$ and V_0 can be computed accurately for larger times; the stronger curvature effect means that finger formation, and consequent crowding, take longer to develop.
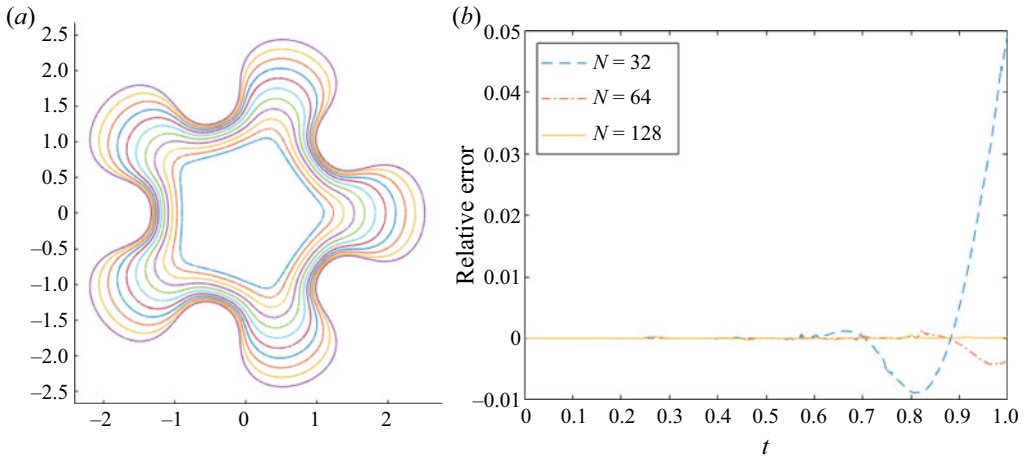
Figure 3. (*a*) Evolution of fire fingers for a fire-star $n = 5$ with $V_0 = 0$, $\bar{\epsilon} = 0.1$, $Pe_0 = 2$, $\lambda = 0$, $\sigma_0 = 0.05$, $N = 128$ and $t_{max} = 1$. (*b*) Relative error of the rate of change of area law (4.8) of plot (*a*), for varying N.
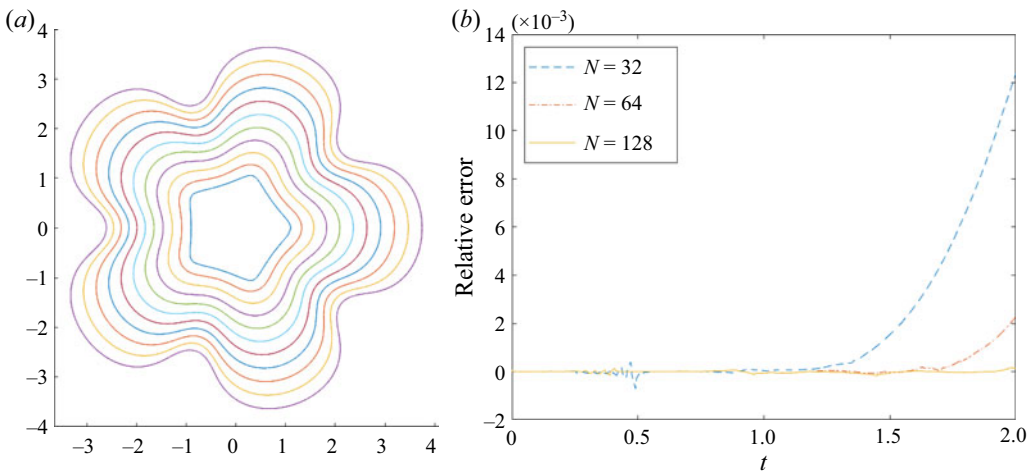

Figure 4. (*a*) Evolution of fire fingers for a fire-star $n = 5$ with $V_0 = 1$, $\bar{\epsilon} = 0.5$, $Pe_0 = 5$, $\lambda = 0.2$, $\sigma_0 = 0.1$, $N = 128$ and $t_{max} = 2$. (*b*) Relative error of the rate of change of area law (4.8) of plot (*a*), for varying N.

Figure 4(*a*) gives an example of a more stable case; its initial state is the same as that of figure 3(*a*), but now with $V_0 = 1$, $\bar{\epsilon} = 0.5$, $\lambda = 0.2$ and $\sigma_0 = 0.1$, and evolving up to a time $t_{max} = 2$. The burned area R grows to a larger size due to the non-zero V_0, and though fingers still develop as predicted in the stability diagram figure 2(*b*) (point B), they are less pronounced compared with figure 3(*a*), due to the V_0 and increased $\bar{\epsilon}$ effects. Also, the relative errors plotted in figure 4(*b*) are significantly smaller in magnitude than those in figure 3(*b*), with *RE* decreasing as N is increased. Henceforth, all plots will use $N = 128$, unless stated otherwise.

The result of increasing the curvature effect is shown in figure 5 for four choices of $\bar{\epsilon}$. As expected (Sethian 1985; Hilton *et al.* 2016), increasing $\bar{\epsilon}$ smooths the fire line, reducing the amplitude of the fingers and valleys. The value $\lambda = 0.2$ is chosen, hence the stability diagram figure 2(*b*) is considered, with figures 5(*a–d*) corresponding to the points C, B,
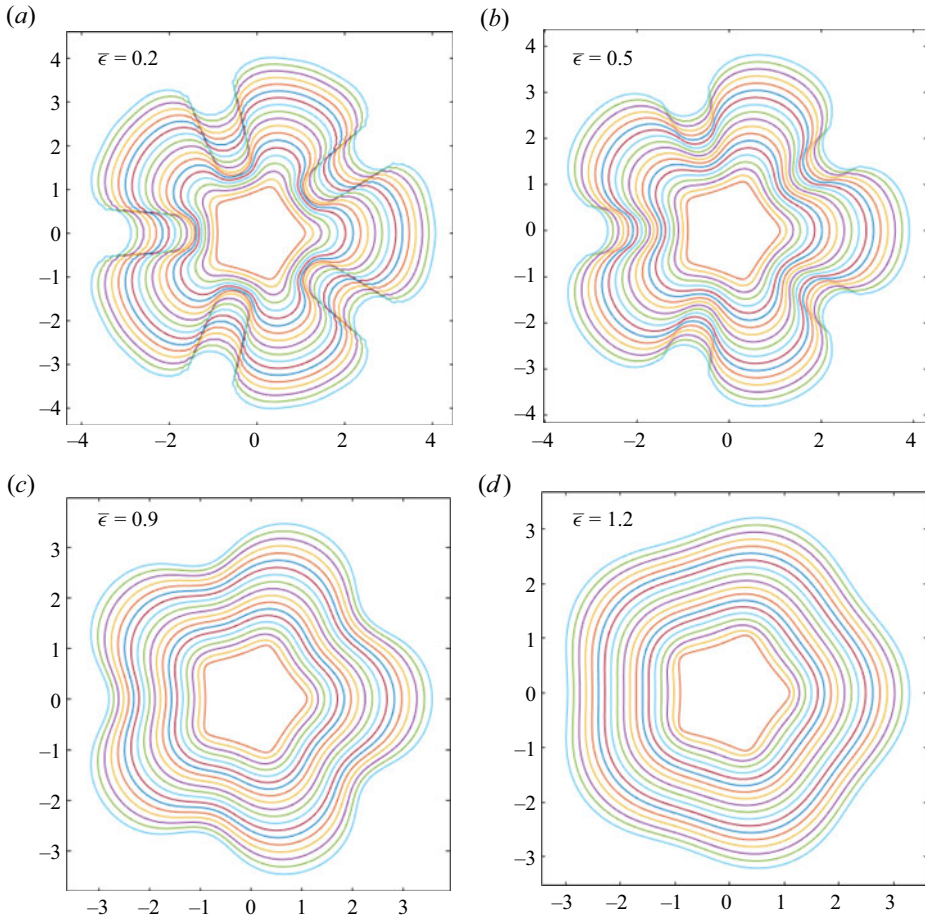
943 A34-13

Figure 5. The effect of increasing $\bar{\epsilon}$: evolution of a fire-star with $n = 5$, $V_0 = 1$, $Pe_0 = 5$, $\lambda = 0.2$, $N = 128$, $t_{max} = 2$ and: (a) $\bar{\epsilon} = 0.2$, $\sigma_0 = 0.04$; (b) $\bar{\epsilon} = 0.5$, $\sigma = 0.1$; (c) $\bar{\epsilon} = 0.9$, $\sigma = 0.18$; (d) $\bar{\epsilon} = 1.2$, $\sigma = 0.24$.

D and E, respectively. Figures 5(a,b) are unstable, and figure 5(d) is stable, in agreement with the initial position of each experiment in figure 2(b).

However, in figure 5(c), while perturbations seem to decay at first, eventually the fingers grow to an amplitude larger than the initial perturbations. Considering figure 2(b), the fire starts at point D in the stability region, but as σ decreases, the fire enters the instability regime. This is known as a 'dormant fire instability', as the fire fingers appear to recede before growing again. Eventually, any initially stable fire line will become unstable as Pe will continue to grow; the physical likelihood of this is discussed in § 6. Figure 6(a) gives an example of a dormant fire instability of a 7-pointed ($n = 7$) fire-star. The corresponding translation of the fire line on the stability diagram is also shown in figure 6(b) as a white line with markers at each time step of 1.25. The value of λ is zero, and initially, $\sigma = 0.25$, so the fire line is stable at $t = 0$ and perturbations decay. At $t = 1.25$, perturbations start to grow, but are slower than the overall growth of the wildfire; the fire line does not become unstable until around $t = 1.8$, when $\sigma = 0.106$. However, fire fingers do not become apparent until $t = 5$.

Finally, the effect of increasing V_0 on fire line evolution is shown in figure 7, where figures 7(a–d) correspond to the points F, B, G and H in figures 2(a–d), respectively.
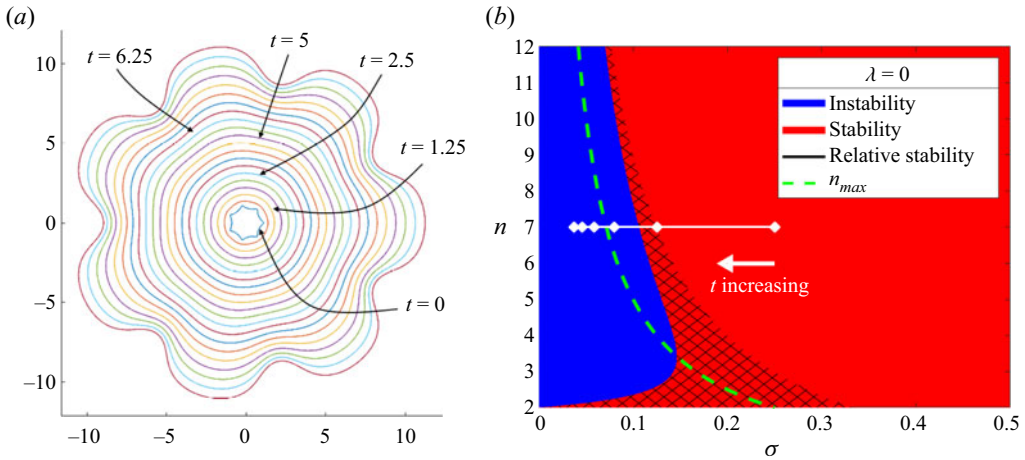
Figure 6. (*a*) The evolution of a dormant fire instability of a 7-pointed star with $n = 7$, $V_0 = 0$, $\bar{\epsilon} = 0.5$, $Pe_0 = 2$, $\lambda = 0$, $\sigma_0 = 0.25$, $N = 128$ and $t_{max} = 10$. (*b*) The parameter space stability diagram of (*a*); each marker represents a time step of $t = 1.25$, from $t = 0$ (furthest right) to $t = 6.25$ (furthest left).

Increasing V_0 in the stability diagrams of figure 2 'thins' and shifts the instability region such that instability is not achieved until smaller values of σ are reached, and some lower modes, such as $n = 3$, may always be relatively stable. In the case of fire-stars ($n = 5$) with $\lambda \leqslant 2$, however, instability is always eventually realised. Note that although figure 7(*d*) looks almost circular, distinct valleys are still observed; increasing V_0 causes fire fingers to widen, but not necessarily to flatten.

4.3.2. *Fire lines with elliptical starting shapes*

In addition to slightly perturbed circular fire lines (as in § 3), for example the fire-stars previously considered, the numerical method is also able to compute the evolution of fire lines with non-small initial perturbations. For the sake of illustration, here elliptical starting shapes are considered, that is, γ is a 2-fold ($n = 2$) symmetric curve that corresponds to an ellipse with eccentricity e. As $e \to 1$, the minor axis of the ellipse approaches 0, so the ellipse tends towards a slit. Choosing an eccentricity close to 1 provides an approximation of the evolution of a one-dimensional fire line segment. As perturbations are non-small, the stability analysis of § 3 is not relevant in this case.

Figure 8 shows a series of results for initial ellipses with $e = 0.9986$, all of which use $N = 128$, $t_{max} = 9$ and $Pe_0 = 2$. The effect of increasing V_0 is shown in figures 8(*a–c*). As in figure 7 for a fire-star, the fires grow to a larger conformal radius as V_0 increases, as noted by the axis scales in each figure. There is also evidence of finger widening; however, as there are only two fingers, this is seen as the valley between the fingers decreasing in depth and width, but still the valley is preserved. Flattening of the fingers is achieved by increasing the curvature effect, as seen in figure 8(*d*), where $\bar{\epsilon}$ has increased to 0.9, as opposed to 0.5 for the other plots in figure 8. Finally, numerical instabilities are visible in figure 8(*a*) at around $t = 7$, due to the high curvature of the developing valleys. The model fails when the fire line begins to intersect previous iterations of itself from $t = 8$ onwards. This violates the entropy condition (Sethian 1985), hence the results are unphysical from this time; results are displayed up to $t_{max} = 9$ to show the self-intersection of the fire line more clearly.
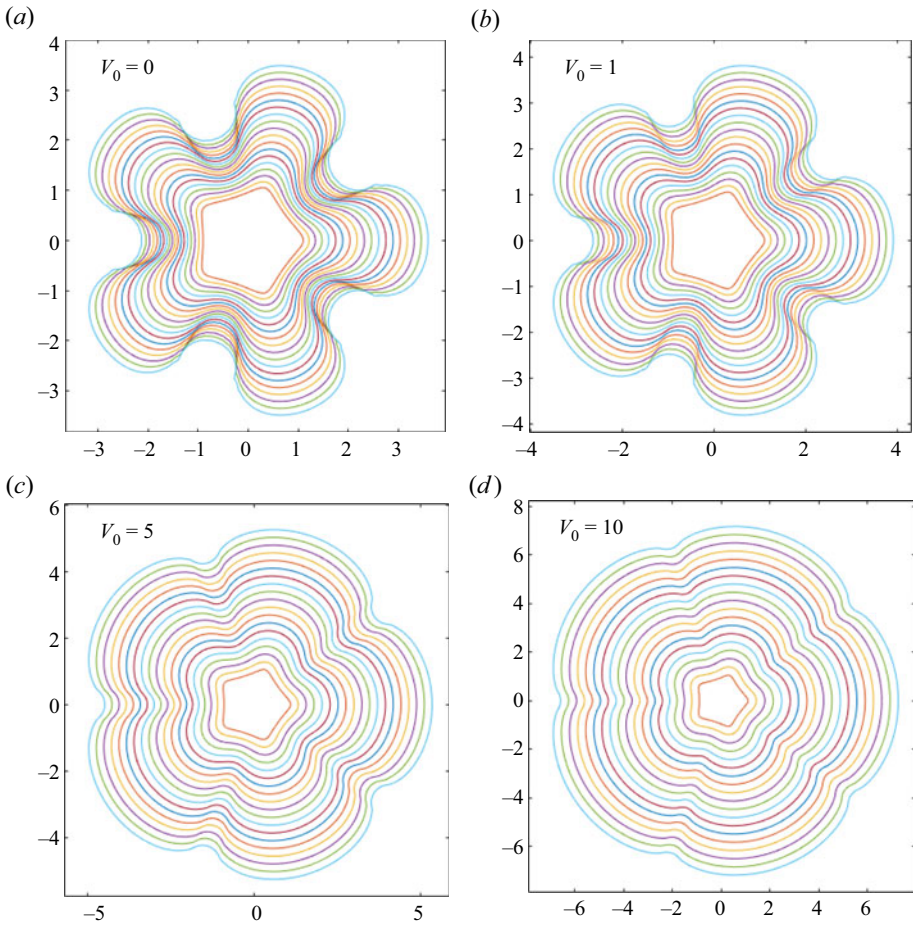
Figure 7. The effect of increasing V_0: evolution of a fire-star with $\bar{\epsilon} = 0.5$, $Pe_0 = 5$, $N = 128$, $t_{max} = 2$ and: (a) $V_0 = 0$, $\lambda = 0$; (b) $V_0 = 1$, $\lambda = 0.2$; (c) $V_0 = 5$, $\lambda = 1$,; (d) $V_0 = 10$, $\lambda = 2$.

4.3.3. *Emergence of a dominant mode*

So far, only one mode of perturbation has been induced on a circular fire line; for fire-stars, this was the mode $n = 5$ (or $n = 7$ for a 7-pointed star), and for an ellipse it was $n = 2$. Now, multiple modes of (small) perturbation will be imposed at once, and the resulting evolution explored. To allow many (co-prime) modes to be added, only 1-fold symmetry ($n = 1$) is assumed; this means that the coefficients of (4.2) are still real and hence solvable in the current numerical method. It is expected that one mode will eventually dominate, for example the mode $n = n_{max}$ (see § 3) that has the highest growth rate g_{max} of all possible modes for a given σ. In general, the mode with the highest growth rate of all excited modes will dominate. Since the Péclet number is increasing, and so σ is decreasing, this dominant mode changes over time, as noted in § 3.

First consider the case where Pe is a constant in time; this differs from the radial fire model but means that the values of σ, and hence n_{max}, are unchanging. Much of the working remains the same as in § 3, with $\sigma = \bar{\epsilon}/Pe = \text{const.}$, and the only difference to the governing equation (4.5) is a -1 term rather than $-a_{-1}(t)$. Perturbations incorporating $n = 3$, 5 and 7 modes are induced, each of small and equal amplitude, to an initially
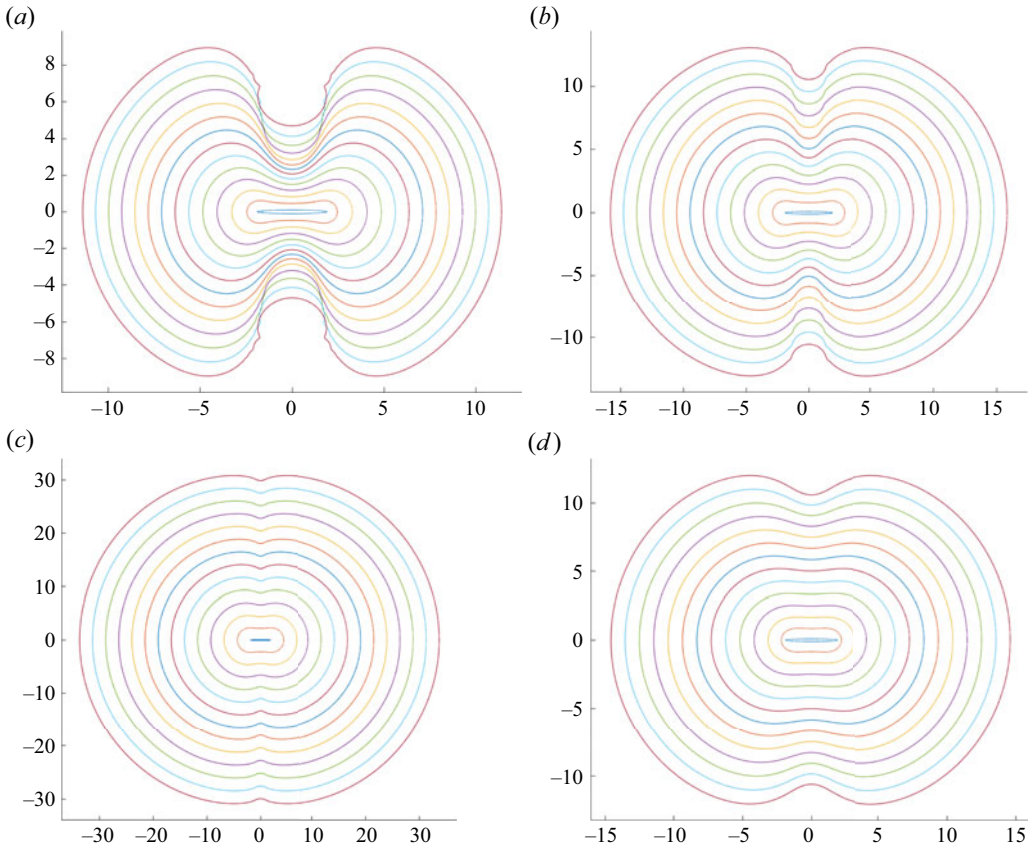
943 A34-16

Figure 8. Evolution of an initially elliptical fire line with $Pe_0 = 2$, $N = 128$, $t_{max} = 9$, $e = 0.9986$ and: (a) $V_0 = 0$, $\bar{\epsilon} = 0.5$, $\sigma_0 = 0.25$; (b) $V_0 = 1$, $\bar{\epsilon} = 0.5$, $\sigma_0 = 0.25$; (c) $V_0 = 5$, $\bar{\epsilon} = 0.5$, $\sigma_0 = 0.25$; (d) $V_0 = 1$, $\bar{\epsilon} = 0.9$, $\sigma_0 = 0.45$.

circular fire line. Fire line evolution is computed up to $t_{max} = 9$ with zero ROS ($V_0 = 0$) and a series truncation $N = 128$. Figures 9(a–c) show the results for the different choices of $\sigma = 0.08$, 0.1 and 0.14, respectively. In each plot, a different dominant mode emerges: when $\sigma = 0.08$ (figure 9a), the 7th mode dominates; for $\sigma = 0.1$ (figure 9b), it is the 5th mode; and (c) for $\sigma = 0.14$ (figure 9c), it is the 3rd mode. This agrees with the stability diagram in figure 9(d); for each choice of σ, the positions of the 3rd-, 5th- and 7th-order perturbations are plotted as nodes. For $\sigma = 0.1$, $n = 5$ is exactly n_{max}. For $\sigma = 0.08$, $n = 7$ has the highest growth rate of the three perturbations and hence dominates; and similarly for $n = 3$ in the $\sigma = 0.14$ case.

Now consider when $Pe = Pe_0 \, a_{-1}(t)$. As σ decreases, the value of n_{max} (see (3.16a)) increases, so it is expected that the highest numbered excited mode will dominate eventually – though it should be cautioned that once perturbations grow sufficiently large, they are no longer 'small' and so the stability analysis of § 3 can no longer be expected to hold. Numerical experiments in figure 10 show the evolution of the same initial fire line as in figure 9, with the same initial conditions $V_0 = 0$ and $N = 128$, but with different choices of σ_0. The value of t_{max} in each experiment corresponds to the maximum time possible before the simulation fails.
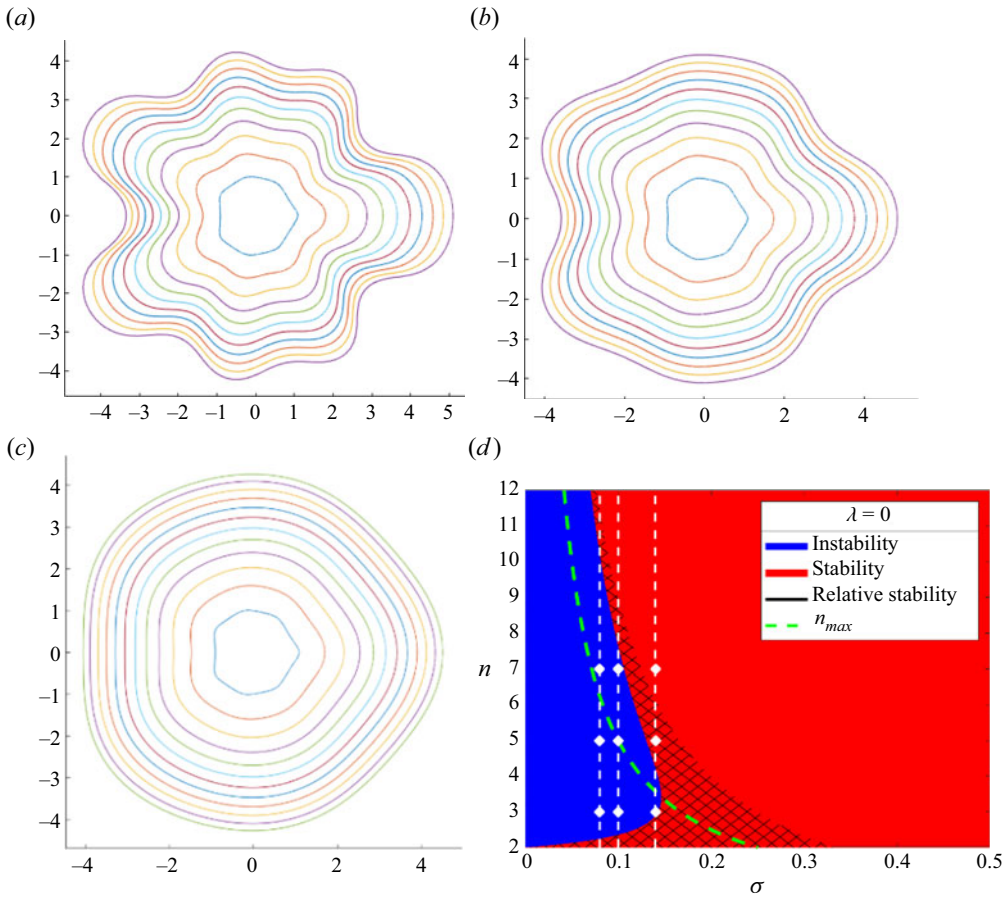
Figure 9. (*a–c*) Evolution of a fire line with 3rd-, 5th- and 7th-order perturbations and *Pe* constant. Here, $V_0 = 0, Pe_0 = 5, \lambda = 0, t_{max} = 9, N = 128$, and (*a*) $\sigma = 0.08$, (*b*) $\sigma = 0.1$, (*c*) $\sigma = 0.14$. (*d*) Stability diagram; each vertical, dashed line represents the σ value for results in (*a–c*) (from left to right), and each node on these vertical lines represents the 3rd-, 5th- and 7th-order perturbation terms.

There is immediately a difference compared to the constant *Pe* case. Figure 10(*a*) has the same starting value $\sigma_0 = 0.14$ as in figure 9(*c*), yet now the 7th-order perturbation dominates, not the 3rd, with the final value of σ as $\sigma_f = 0.04$. The fire fingers grow faster too, achieving a similar result to figure 9(*a*) but at a quicker time $t = 2.5$. Any lower initial values of σ_0 also result in the 7th-order perturbation dominating. In figure 10(*b*), $\sigma_0 = 0.2$, and it is the 5th-order perturbation that dominates, with the simulation terminating at $t_{max} = 5.2$ when $\sigma_f = 0.033$. The fact that this mode dominates over the higher $n = 7$ mode seems to contradict what is expected, though it is likely that the numerical method ended before the $n = 7$ mode could begin to grow sufficiently. Close inspection of figure 10(*b*) suggests that there are in fact seven fingers growing, not five.

5. Periodic infinite fire lines

Infinite fire lines are now considered, and this can be thought of as studying a sufficiently large wildfire at a local scale. In particular, a periodic curve γ_L is considered over one period $[-L\pi, L\pi]$, with L a characteristic length scale used to convert to
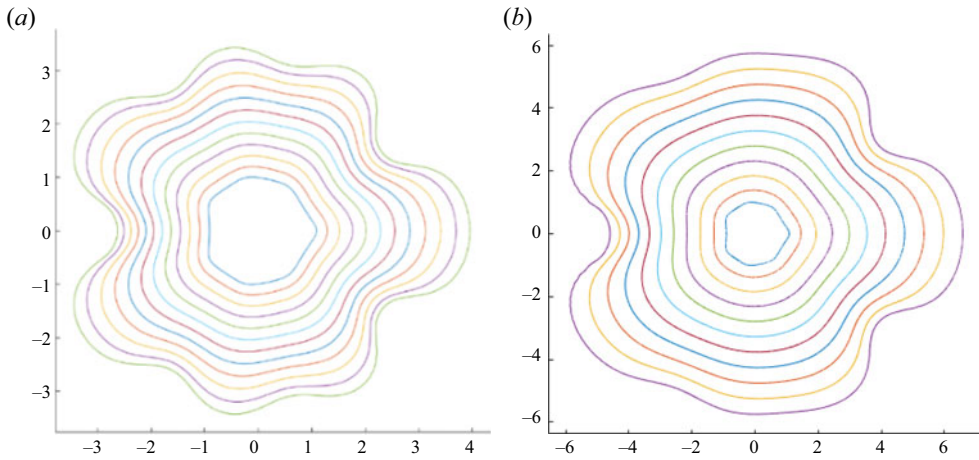
943 A34-18

(a)

(b)

Figure 10. Evolution of the initial fire line in figure 9 for a time-dependent *Pe*, with $V_0 = 0$ and $N = 128$: (a) $\sigma_0 = 0.14$, $\sigma_f = 0.04$, $t_{max} = 2.5$; (b) $\sigma_0 = 0.02$, $\sigma_f = 0.033$, $t_{max} = 5.2$.
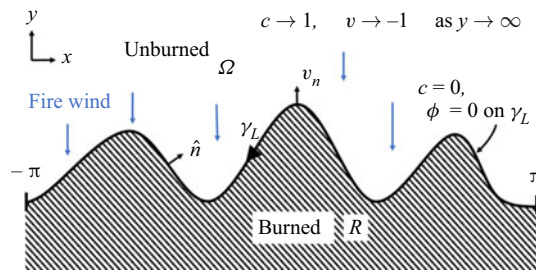

Figure 11. The dimensionless wildfire problem for a periodic infinite fire line.

non-dimensional quantities. The dimensionless system (2.8)–(2.12) used for radial fire lines also holds in the periodic infinite case, but with two main changes. First, as a local scale is considered, it is assumed that the strength Q of the fire plume remains constant over time as the fire line propagates forward. Therefore, the Péclet number is also constant, hence $Pe = Pe_0$ always. Second, the far-field condition (2.12*b*) is now that of a uniform flow in the negative $\hat{y}$ direction, as the effective oxygen sink is now on the line $y = R(t)$, which draws in oxygen-rich air from the unburned region at $y \to +\infty$. Note that $R(t)$ is not a radius; rather, it is the horizontal line $y = R(t)$.

The non-dimensional system for periodic infinite fire lines is thus

$$Pe\, v_n = V_0 - \bar{\epsilon}\kappa + \hat{n} \cdot \nabla c \quad \text{on } \gamma_L, \tag{5.1}$$

$$\nabla^2 \phi = 0 \quad \text{in } \Omega, \tag{5.2}$$

$$Pe\, \boldsymbol{u} \cdot \nabla c = \nabla^2 c \quad \text{in } \Omega, \tag{5.3}$$

$$c = 0, \quad \phi = 0 \quad \text{on } \gamma_L, \tag{5.4a,b}$$

$$c \to 1, \quad v \to -1 \quad \text{as } y \to \infty. \tag{5.5a,b}$$

The problem is shown diagrammatically in figure 11.

5.1. *Stability analysis*

As in § 3, consider first an unperturbed base case $y = R(t)$. Assuming that ϕ and c are independent of x, the following solve (5.1)–(5.5a,b):

$$\phi(y) = R(t) - y, \quad c(y) = 1 - \exp(Pe\,(R(t) - y)). \tag{5.6a,b}$$

Next, perturbations $y = y_p = R(t) + \delta_n \cos nx$ are added, where the summation sign has been dropped and $\delta_n \ll 1$, for all $n = 1, 2, 3, \ldots$. Note that $n = 1$ is not a simple translation as in the radial case, hence perturbations $n \geqslant 1$ are retained here. The following solutions for ϕ and c are assumed:

$$\left.\begin{aligned}
\phi(x, y) &= R(t) - y + \beta_n \exp(n(R(t) - y)) \cos nx, \\
c(x, y) &= 1 - \exp(Pe\,(R(t) - y)) + \gamma_n \exp(\alpha_n(R(t) - y)) \cos nx,
\end{aligned}\right\} \tag{5.7}$$

with constants $\beta_n, \gamma_n \ll 1$ and α_n. Substitution of (5.7) into (5.3) and (5.4a,b) gives $\beta_n = \delta_n$, $\gamma_n = -Pe\,\delta_n$ and $\alpha_n = n + Pe$.

The normal velocity (2.8) can be written in terms of y_p as

$$Pe\,(\dot{R} + \dot{\delta}_n \cos nx) = V_0 - \bar{\epsilon}n^2\delta_n \cos nx + Pe\,[1 + n\delta_n \cos nx]. \tag{5.8}$$

Extracting the first-order terms gives

$$Pe\,\dot{R} = V_0 + Pe, \tag{5.9}$$

and an exact solution for R can be found:

$$R(t) = (\lambda + 1)t, \tag{5.10}$$

where $\lambda = V_0/Pe$ and the condition $R(0) = 0$ has been imposed. The relative growth of the fire line is therefore

$$\frac{\dot{R}}{R} = \frac{1}{R}(\lambda + 1) = \frac{1}{t}, \tag{5.11}$$

which eliminates the parameter λ, and thus V_0, from the stability analysis. Next, the $O(\delta_n)$ terms from (5.8) are taken, giving

$$Pe\,\dot{\delta}_n = -\bar{\epsilon}n^2\delta_n + n\,Pe\,\delta_n, \tag{5.12}$$

thus

$$\frac{\dot{\delta}_n}{\delta_n} = n(1 - \sigma n), \tag{5.13}$$

where $\sigma = \bar{\epsilon}/Pe$ is a constant in time.

Therefore the relative growth rate is

$$g(n) = \frac{\partial}{\partial t}\left(\log\left(\frac{\delta_n}{R}\right)\right) = \frac{\dot{\delta}_n}{\delta_n} - \frac{\dot{R}}{R} = n(1 - \sigma n) - \frac{1}{t}. \tag{5.14}$$

As in § 3, $g(n) > 0$ is unstable behaviour, $g(n) \leqslant 0$ implies stability, and 'relative stability' is when $\dot{\delta}_n/\delta_n > 0$ but $g(n) \leqslant 0$. Care must also be taken at $t = 0$, though it is only the sign of (5.14) that is important, so state simply that $g < 0$ at $t = 0$, for all n. Whereas the growth rate of radial fires (3.11) was variable in n and σ, with σ decreasing over time, now σ is a constant and the growth rate for periodic infinite fire lines (5.14) is explicitly
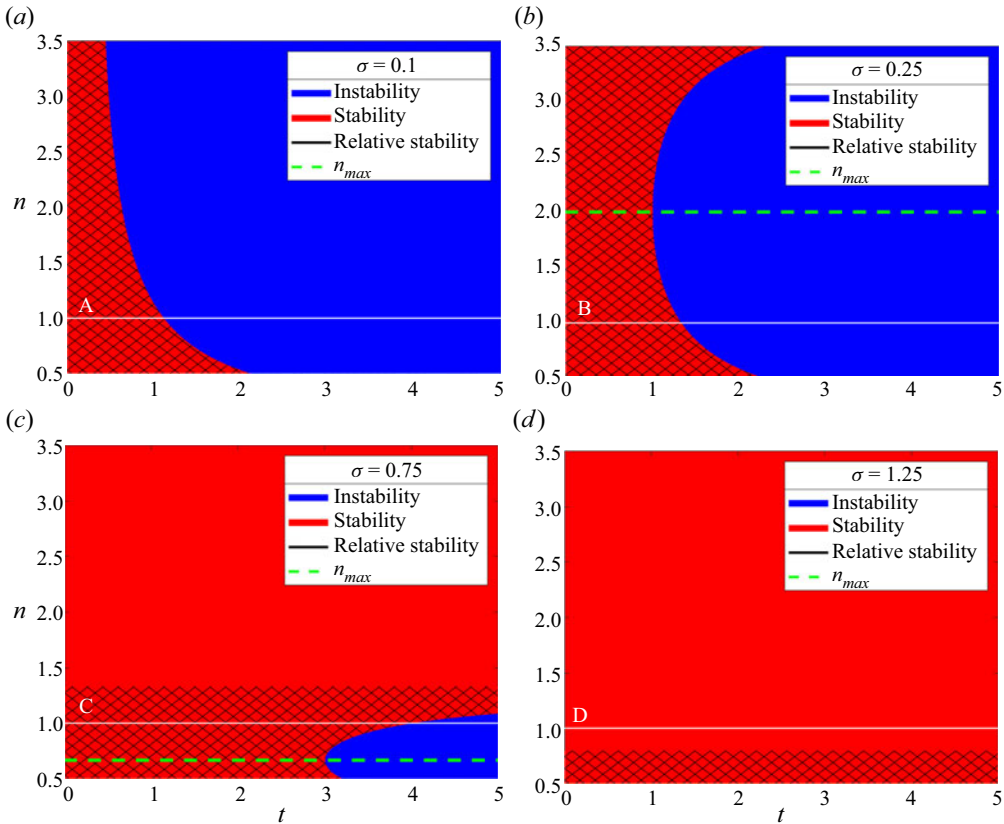
Figure 12. Parameter space stability diagrams for the perturbed periodic infinite fire line. The cross-hatched areas (denoted by the black line in the graph key) are regions of 'relative stability'. The lines A–D represent upcoming numerical results, which run from $t = 0$ to $t = 5$, as follows: A – figure 13(*a*); B – figures 13(*b*) and 14; C – figure 13(*c*); D – figure 13(*d*).

time-dependent, approaching the standard growth rate (5.13) as t increases. Therefore, the resulting stability diagrams, as given in figure 12, have axes n versus t, rather than n versus σ, with a constant value of σ chosen for each plot. The maximum growth rate g_{max} and its corresponding mode n_{max} are also found as

$$n_{max} = \frac{1}{2\sigma}, \quad g_{max} = \frac{1}{4\sigma} - \frac{1}{t}. \tag{5.15a,b}$$

The lines A–D identified in figure 12 correspond to upcoming numerical results that all run from $t = 0$ to $t = 5$, i.e. tracing from left to right on the stability diagram.

5.2. *Numerical results*

The conformal mapping method from § 4.1 is used again to produce numerical results. For one period of a periodic infinite fire line, the following conformal map from the interior of the unit ζ-disk to the unburned region Ω is used:

$$z = f(\zeta, t) = -\mathrm{i} \log \zeta + \mathrm{i}\, a_0(t) + \mathrm{i} \sum_{m=1}^{\infty} a_m(t)\, \zeta^m. \tag{5.16}$$
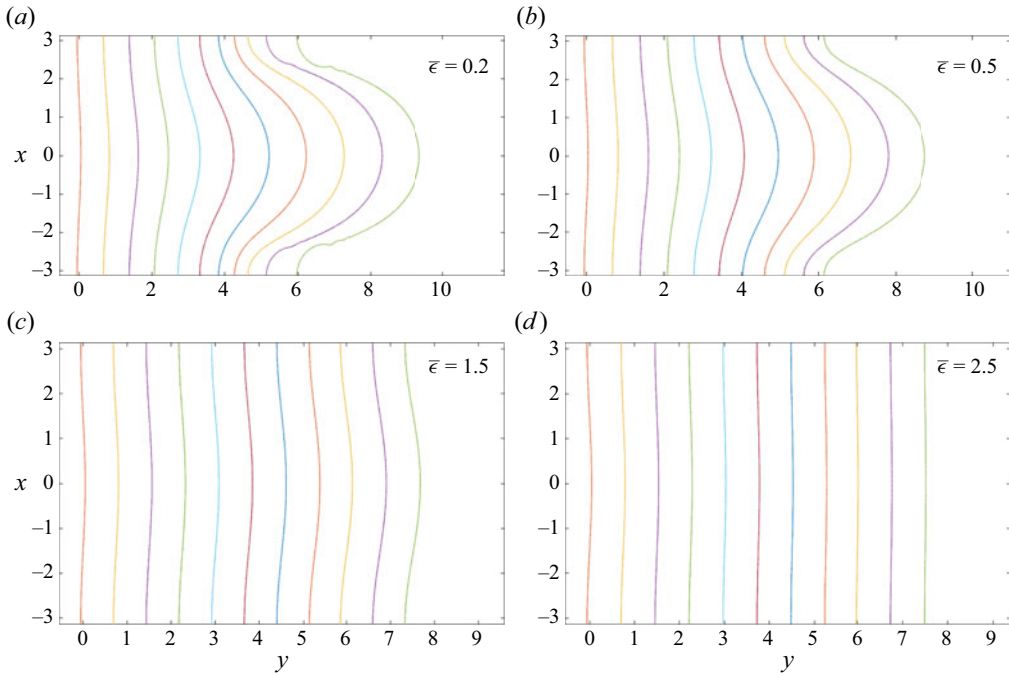
Figure 13. The effect of increasing $\bar{\epsilon}$: evolution of a periodic infinite fire line with $V_0 = 1$, $Pe = 2$, $N = 128$, $t_{max} = 5$ and: (a) $\bar{\epsilon} = 0.2$, $\sigma = 0.1$; (b) $\bar{\epsilon} = 0.5$, $\sigma = 0.25$; (c) $\bar{\epsilon} = 1.5$, $\sigma = 0.75$; (d) $\bar{\epsilon} = 2.5$, $\sigma = 1.25$.

Symmetry about the y-axis is assumed, so the unknowns a_m are real.

The normal velocity v_n (see (5.1)) is evaluated as in § 4 to give

$$\text{Re}\left[f_t\overline{\zeta f_\zeta}\right] = -\frac{V_0}{Pe}\,|f_\zeta| + \frac{\bar{\epsilon}}{Pe}\,\frac{\text{Re}\left[\zeta(\zeta f_\zeta)_\zeta\,\overline{\zeta f_\zeta}\right]}{|f_\zeta|^2} - 1, \tag{5.17}$$

with the -1 term rather than the $a_{-1}(t)$ in (4.5), as Pe is now not scaled in time. For all upcoming results, the initial fire line is a straight-line segment with a simple 'bump', i.e. a perturbation of $n = 1$. Also, the axes have been inverted (y is the horizontal) to show the evolution more clearly.

Figure 13 shows the effect of increasing the curvature by comparing the values $\bar{\epsilon} = 0.2, 0.5, 1.5$ and 2.5, with $Pe = 2$, $V_0 = 1$, $N = 128$ and $t_{max} = 5$ for all plots. Similar to radial fire line evolution, such as in figures 13(a,b), as the curvature effect increases, the finger grows more slowly until eventually the curvature is strong enough to stop finger growth altogether as in figure 13(d). Note also that for small curvature, e.g. in figure 13(a) ($\bar{\epsilon} = 0.2$), numerical instabilities appear eventually. This is again likely due to crowding. Considering stability, figures 13(a–d) correspond to the lines A, B, C and D across the stability diagrams figures 12(a–d), respectively. The only stable solution is in figure 13(d), where $\bar{\epsilon} = 2.5$; this is in agreement with figure 12, as line D is the only experiment never to enter the instability region for $0 \leqslant t \leqslant 5$.

Figure 14 shows the effect of increasing the ROS, comparing the values $V_0 = 0, 1, 2, 5$, with $Pe = 2$, $\bar{\epsilon} = 0.5$, $\sigma = 0.25$, $N = 128$ and $t_{max} = 5$ for all plots. All figures correspond to and agree with the line B in the stability diagram figure 12(b), showing that each result is unstable after the first few time steps. Increasing V_0 causes the fire line to propagate faster and the finger to widen; the finger in figure 14(d) covers almost the entire period.
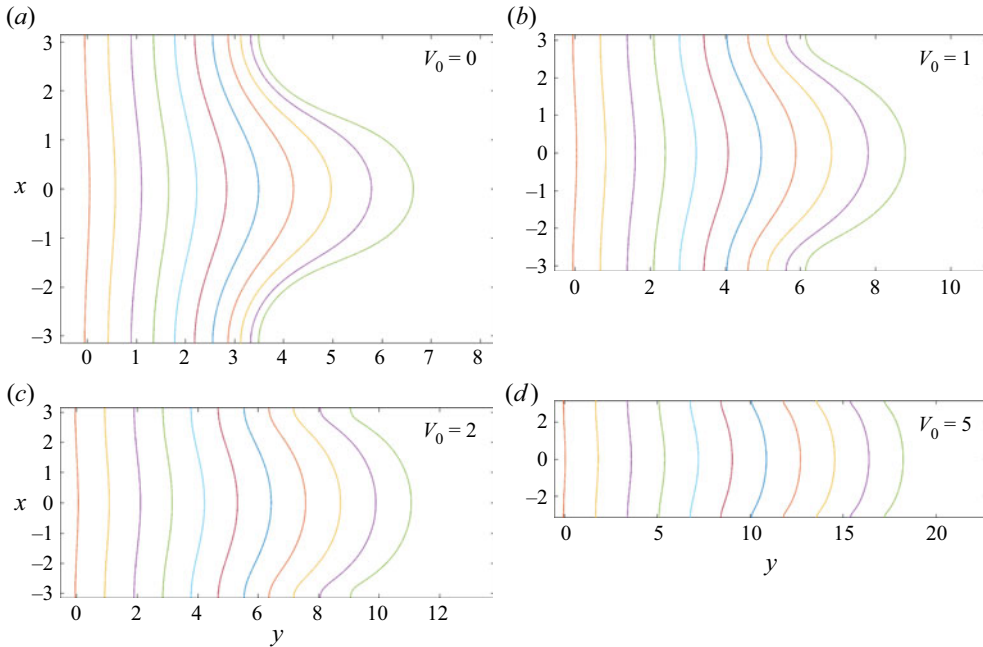
943 A34-22

Figure 14. The effect of increasing V_0: evolution of a periodic infinite fire line with $\bar{\epsilon} = 0.5$, $Pe = 2$, $\sigma = 0.25$, $N = 128$, $t_{max} = 5$, and (a) $V_0 = 0$, (b) $V_0 = 1$, (c) $V_0 = 2$, (d) $V_0 = 5$.

6. Discussion

The stability and nonlinear evolution of radial and infinite fire lines have been considered using a two-dimensional model incorporating both geometric and dynamic effects. Fingering instabilities are possible for certain values of σ, the ratio between curvature $\bar{\epsilon}$ (stabilising) and oxygen Pe (destabilising) effects, and numerical results demonstrate both stable and unstable fire line growth. A third type of behaviour was also found: 'dormant fire' behaviour, where fire finger growth would change from stable to unstable over time. This was a consequence of an increasing Péclet number in the radial case. In cases where multiple modes of perturbation were excited, the mode with the highest growth rate would dominate eventually. Consequently, geometrically identical initial fire lines evolve into different fire finger patterns, depending on the value of σ.

Using $L \approx 20$ m for the initial size of a radial fire that generates a fire wind of 0.025 m s^{-1} gives an initial estimate $Q = 2\pi \times 0.5$ m^2 s^{-1}. These values are consistent with large-scale experimental grass fires reported in Hilton *et al.* (2018). Bebieva *et al.* (2020) estimate that within 1 m of ground level, the horizontal diffusivity D in fire conditions is $O(1)$ m^2 s^{-1}, although the actual value will depend on vegetation type, among other factors. Hence $Pe_0 = Q/2\pi D \approx 0.5$. The value of $\bar{\epsilon}$ is more difficult to estimate. In the combustion wind tunnel experiments discussed by Hilton *et al.* (2016) (see e.g. their figure 6), fires typically have length scale 0.5 m, and they found by comparison with their numerical experiments (which included curvature) that dimensionally, the curvature term's contribution to the normal velocity is $\approx 2 \times 10^{-4}$ m s^{-1}. In the same experiments, a typical fire line velocity in the absence of wind was 3×10^{-3} m s^{-1}, so $\bar{\epsilon} \approx 0.1$. Thus choosing this value as being representative of larger scale fire, it follows that $\sigma_0 = \bar{\epsilon}/Pe_0 \approx 0.2$. With caveats about applying these estimates to larger-scale

943 A34-23

fires and questions about how different fuel types and vegetation affect wildfires, the estimate for σ_0 suggests that fingering owing to the oxygen effect is a possibility in actual wildfires.

The fire line normal velocities (2.8) and (5.1) are extensions of the curvature flow models used by e.g. Sharples *et al.* (2013) and Sethian (1985), with the added term $\hat{\boldsymbol{n}} \cdot \nabla c$ modelling the effect of additional oxygen supplied to the fire by advection and diffusion. While the diffusion and advection of oxygen concentration in relation to fires has been acknowledged (Zik *et al.* 1998; Conti & Marconi 2002), and the phenomenon of fire wind is well known (Smith *et al.* 1975; Beer 1991; Hilton *et al.* 2018), the explicit inclusion of the oxygen term in the normal velocity of the fire line is new. Mathematically, the model combines aspects of curve-shortening flow (Dallaston & McCue 2016), fingering in a Hele-Shaw cell in the absence of surface tension (Howison 1986; Mineev-Weinstein 1998; Gustafsson & Vasil'ev 2006), and two-dimensional melting/freezing free-boundary problems featuring the advection–diffusion equation (2.10) (e.g. Cummings *et al.* 1999; Rycroft & Bazant 2016; Ladd *et al.* 2020).

Several extensions to the model are of interest. Wildfires are affected strongly by ambient winds, and their inclusion would give rise to two effects. The first is a contribution to the ROS, taking the form $\boldsymbol{V} \cdot \hat{\boldsymbol{n}}$, where V is the ambient wind, while taking care to ensure that the fire line does not turn back on itself towards the burned region (e.g. Hilton *et al.* 2018). The second effect is the ability of an ambient wind to transport additional oxygen to the fire line. Interestingly, Beer (1991) argues that in the presence of an ambient wind, the fire wind generated by the rising hot air over the burned region is reduced, and in turn, so is the instability mechanism of enhanced oxygen at the fire front. Depending on their direction, ambient winds may also transport oxygen from the burned regions to the fire line. This provides a stabilising effect since now the finger tips receive comparatively less oxygen than the valleys between fingers.

Other effects that are possible to incorporate into the model include the variance of ROS depending on whether the fire is propagating upslope or downslope, and the effect of inhomogeneous fuel and firebreaks. All these effects can be modelled by spatially dependent normal velocities, and are relatively straightforward to include in the numerical technique. To enable accurate computation of fire line evolution over longer times, an approach based on approximating the fire line as a many-sided polygon in which nodes can be added (or subtracted) according to local curvature, and in which fire lines can merge, is being developed presently. Consideration of the fire line as a polygon means that it can be mapped numerically to a canonical domain in order to facilitate the calculation of the oxygen diffusion and advection effect.

In real wildfires, fire fingers are only occasionally observed, despite the prediction here that all radial fires must eventually become unstable as *Pe* increases with fire size. In reality, it seems likely that the strength of the fire wind cannot grow indefinitely and that there is a bound on *Pe*, meaning that a fire may remain stable. Moreover, inclusion of additional factors affecting fire spread, such as ambient winds, topography, natural and artificial fire breaks, fuel type and fire spotting, may inhibit or mask finger formation.

Author ORCIDs.

S.J. Harris https://orcid.org/0000-0003-2517-7980;

N.R. McDonald https://orcid.org/0000-0002-3595-7377.

REFERENCES

ACHTEMEIER, G.L. 2012 Field validation of a free-agent cellular automata model of fire spread with fire–atmosphere coupling. *Intl J. Wildland Fire* **22** (2), 148–156.

BAKHSHAII, A. & JOHNSON, E.A. 2019 A review of a new generation of wildfire–atmosphere modeling. *Can. J. Forest Res.* **49** (6), 565–574.

BAZANT, M.Z. 2004 Conformal mapping of some non-harmonic functions in transport theory. *Proc. R. Soc. Lond.* A **460** (2045), 1433–1452.

BEBIEVA, Y., OLIVETO, J., QUAIFE, B., SKOWRONSKI, N.S., HEILMAN, W.E. & SPEER, K. 2020 Role of horizontal eddy diffusivity within the canopy on fire spread. *Atmosphere* **11**, 672.

BEER, T. 1991 The interaction of wind and fire. *Boundary-Layer Meteorol.* **54**, 287–308.

BROWER, R.C., KESSLER, D.A., KOPLIK, J. & LEVINE, H. 1984 Geometrical models of interface evolution. *Phys. Rev.* A **29** (3), 1335–1342.

CLARK, T.L., JENKINS, M.A., COEN, J.L. & PACKHAM, D.R. 1996*a* A coupled atmosphere–fire model: convective feedback on fire-line dynamics. *J. Appl. Meteorol. Clim.* **35** (6), 875–901.

CLARK, T.L., JENKINS, M.A., COEN, J.L. & PACKHAM, D.R. 1996*b* A coupled atmosphere–fire model: role of the convective Froude number and dynamic fingering at the fireline. *Intl J. Wildland Fire* **6** (4), 177–190.

CONTI, M. & MARCONI, U.M.B. 2002 Fingering in slow combustion. *Physica* A **312** (3), 381–391.

CONTI, M. & MARCONI, U.M.B. 2010 Diffusion limited propagation of burning fronts. In *Modelling, Monitoring and Management of Forest Fires II* (ed. G. Perona & C.A. Brebbia), pp. 37–45. WIT.

CUMMINGS, L.M, HOHLOV, Y.E., HOWISON, S.D. & KORNEV, K. 1999 Two-dimensional solidification and melting in potential flows. *J. Fluid Mech.* **378**, 1–18.

DALLASTON, M.C. & HEWITT, I.J. 2014 Free-boundary models of a meltwater conduit. *Phys. Fluids* **26** (8), 083101.

DALLASTON, M.C. & McCUE, S.W. 2013 An accurate numerical scheme for the contraction of a bubble in a Hele-Shaw cell. *ANZIAM J.* **54**, C309–C326.

DALLASTON, M.C. & McCUE, S.W. 2016 A curve shortening flow rule for closed embedded plane curves with a prescribed rate of change in enclosed area. *Proc. R. Soc. Lond.* A **472** (2185), 20150629.

DOLD, J.W., SIVASHINSKY, G. & WEBER, R.O. 2005 Onset of flow-induced fingering in bushfires. In *5th Asia-Pacific Conference on Combustion, Adelaide, Australia* (ed. P. Kalt, G. Nathan & B. Dally), pp. 177–180. The University of Adelaide.

FINNEY, M.A., COHEN, J.D., FORTHOFER, J.M., McALLISTER, S.S., GOLLNER, M.J., GORHAM, D.J., SAITO, K., AKAFUAH, N.K., ADAM, B.A. & ENGLISH, J.D. 2015 Role of buoyant flame dynamics in wildfire spread. *Proc. Natl Acad. Sci. USA* **112** (32), 9833–9838.

GAGE, M. & HAMILTON, R.S. 1986 The heat equation shrinking convex plane curves. *J. Differ. Geom.* **23**, 69–96.

GRAYSON, M.A. 1987 The heat equation shrinks embedded plane curves to round points. *J. Differ. Geom.* **26**, 285–314.

GUSTAFSSON, B. & VASIL'EV, A. 2006 *Conformal and Potential Analysis in Hele-Shaw Cells*. Springer Science & Business Media.

HILTON, J.E., MILLER, C., SHARPLES, J.J. & SULLIVAN, A.L. 2016 Curvature effects in the dynamic propagation of wildfires. *Intl J. Wildland Fire* **25** (12), 1238–1251.

HILTON, J.E., SULLIVAN, A.L., SWEDOSH, W., SHARPLES, J. & THOMAS, C. 2018 Incorporating convective feedback in wildfire simulations using pyrogenic potential. *Environ. Model. Softw.* **107**, 12–24.

HOWISON, S.D. 1986 Fingering in Hele-Shaw cells. *J. Fluid Mech.* **167**, 439–453.

JOLLY, W.M., COCHRANE, M.A., FREEBORN, P.H., HOLDEN, Z.A., BROWN, T.J., WILLIAMSON, G.J. & BOWMAN, D.M. 2015 Climate-induced variations in global wildfire danger from 1979 to 2013. *Nat. Commun.* **6** (1), 7537.

KAGAN, L. & SIVASHINSKY, G. 2008 Pattern formation in flame spread over thin solid fuels. *Combust. Theory Model.* **12** (2), 269–281.

KAYE, N.B. & LINDEN, P.F. 2004 Coalescing axisymmetric turbulent plumes. *J. Fluid Mech.* **502**, 41–63.

LADD, A.J.C., YU, L. & SZYMCZAK, P. 2020 Dissolution of a cylindrical disk in Hele-Shaw flow: a conformal-mapping approach. *J. Fluid Mech.* **903**, A46.

LAREAU, N.P. & CLEMENTS, C.B. 2017 The mean and turbulent properties of a wildfire convective plume. *J. Appl. Meteorol. Clim.* **56** (8), 2289–2299.

MARKSTEIN, G.H. 1951 Experimental and theoretical studies of flame-front stability. *J. Aeronaut. Sci.* **18** (3), 199–209.

MASSON-DELMOTTE, V., *et al.* (Eds) 2021 *IPCC, 2021: Climate Change 2021: The Physical Science Basis. Contribution of Working Group I to the Sixth Assessment Report of the Intergovernmental Panel on Climate Change*. Cambridge University Press.

MAYNARD, T., PRINCEVAC, M. & WEISE, D.R. 2016 A study of the flow field surrounding interacting line fires. *J. Combust.* **2016**, 6927482.

MINEEV-WEINSTEIN, M. 1998 Selection of the Saffman–Taylor finger width in the absence of surface tension: an exact result. *Phys. Rev. Lett.* **80** (10), 2113–2116.

MIRANDA, J.A. & WIDOM, M. 1998 Radial fingering in a Hele-Shaw cell: a weakly nonlinear analysis. *Physica* D **120** (3–4), 315–328.

MULLINS, W.W. & SEKERKA, R.F. 1964 Stability of a planar interface during solidification of a dilute binary alloy. *J. Appl. Phys.* **35** (2), 444–451.

PASTOR, E., ZÁRATE, L., PLANAS, E. & ARNALDOS, J. 2003 Mathematical models and calculation systems for the study of wildland fire behaviour. *Prog. Energy Combust. Sci.* **29** (2), 139–153.

PERRY, G.L.W. 1998 Current approaches to modelling the spread of wildland fire: a review. *Prog. Phys. Geog.* **22** (2), 222–245.

QUAIFE, B. & SPEER, K. 2021 A simple model for wildland fire vortex–sink interactions. *Atmosphere* **12** (8), 1014.

RYCROFT, C.H. & BAZANT, M.Z. 2016 Asymmetric collapse by dissolution or melting in a uniform flow. *Proc. R. Soc. Lond.* A **472** (2185), 20150531.

SETHIAN, J.A. 1985 Curvature and the evolution of fronts. *Commun. Math. Phys.* **101** (4), 487–499.

SHARPLES, J.J. & HILTON, J.E. 2020 Modeling vorticity-driven wildfire behavior using near-field techniques. *Front. Mech. Engng* **5**, 69.

SHARPLES, J.J, TOWERS, I.N., WHEELER, G., WHEELER, V.-M. & MCCOY, J.A. 2013 Modelling fire line merging using plane curvature flow. In *20th International Congress on Modelling and Simulation, Adelaide, Australia*, pp. 256–262.

SMITH, R.K., MORTON, B.R. & LESLIE, L.M. 1975 The role of dynamic pressure in generating fire wind. *J. Fluid Mech.* **68** (1), 1–19.

SULLIVAN, A.L. 2009a Wildland surface fire spread modelling, 1990–2007. 1: Physical and quasi-physical models. *Intl J. Wildland Fire* **18**, 349–368.

SULLIVAN, A.L. 2009b Wildland surface fire spread modelling, 1990–2007. 2: Empirical and quasi-empirical models. *Intl J. Wildland Fire* **18**, 369–386.

SULLIVAN, A.L. 2009c Wildland surface fire spread modelling, 1990–2007. 3: Simulation and mathematical analogue models. *Intl J. Wildland Fire* **18**, 387–403.

TRELLES, J. & PAGNI, P. 1997 Fire-induced winds in the 20 October 1991 Oakland Hills fire. *Fire Safety Sci.* **5**, 911–922.

TSAI, V.C. & WETTLAUFER, J.S. 2007 Star patterns on lake ice. *Phys. Rev.* E **75** (6), 066105.

WEIHS, R.D. & SMALL, D. 1986 Interactions and spreading of adjacent large area fires. *Tech. Rep.* Pacific-Sierra Research Corp., Los Angeles, CA.

WHEELER, V.-M., WHEELER, G.E., MCCOY, J.A. & SHARPLES, J.J. 2015 Modelling dynamic bushfire spread: perspectives from the theory of curvature flow. In *MODSIM2015, 21st International Congress on Modelling and Simulation* (ed. T. Weber, M.J. McPhee & R.S. Anderssen), pp. 319–325. The Modelling and Simulation Society of Australia and New Zealand Inc.

ZIK, O. & MOSES, E. 1999 Fingering instability in combustion: an extended view. *Phys. Rev.* E **60**, 518–531.

ZIK, O., OLAMI, Z. & MOSES, E. 1998 Fingering instability in combustion. *Phys. Rev. Lett.* **81**, 3868–3871.